Boundary-Layer Meteorology
https://doi.org/10.1007/s10546-018-0410-2

RESEARCH ARTICLE

Large-Eddy Simulations of the Flow Over an Isolated Three-Dimensional Hill

Zhenqing Liu[1] · Shuyang Cao[2] · Heping Liu[3] · Takeshi Ishihara[4]

Received: 3 April 2018 / Accepted: 12 November 2018

Abstract
Atmospheric three-dimensional (3D) mean and turbulent flow over an isolated 3D hill of cosine-squared cross-section and a smooth surface are studied by large-eddy simulations validated against data from a wind-tunnel experiment. Many features of the 3D flow across the hill are identified through analyzing mean and turbulent quantities on three surfaces, including a vertical cross-section across the hilltop, and surfaces of vertical distances of $0.25h$ and $1.25h$ from the ground, where h is the hill height. Besides flow blocking and separation with a recirculation region immediately upstream and downstream of the hill, respectively, a spiral-shaped structure wandering in both the lateral and vertical directions develops, accompanied by the wake and shear regions where sweep and ejection events play different roles in momentum transfer. The secondary rotations in the wake flow as well as the inner and outer rotations associated with the core vortex are also identified, together with other features.

Keywords Coherent structures · Large-eddy simulations · Mean and turbulent flow · Three-dimensional hill

✉ Heping Liu
heping.liu@wsu.edu

Zhenqing Liu
liuzhenqing@hust.edu.cn

Shuyang Cao
shuyang@tongji.edu.cn

Takeshi Ishihara
ishihara@bridge.t.u-tokyo.ac.jp

1 School of Civil Engineering and Mechanics, Huazhong University of Science and Technology, Wuhan, Hubei, China

2 State Key Laboratory for Disaster Reduction in Civil Engineering, Tongji University, Shanghai, China

3 Department of Civil and Environmental Engineering, Washington State University, Pullman, WA, USA

4 Department of Civil Engineering, School of Engineering, The University of Tokyo, Tokyo, Japan

Published online: 29 November 2018

1 Introduction

The mean and turbulent flow fields over complex terrain are of great interest for many applications, such as for identifying potential locations of wind turbines (Politis et al. 2012; Bédard et al. 2013; Castro et al. 2014), monitoring pollution dispersion or CO_2 concentration within hilly terrain (Perdikaris 2001; Carvalho et al. 2006; Kutter et al. 2017), estimating the wind loading on buildings or bridges (Davenport and King 1990), identifying regions at high risk of tree damage in windy conditions (Matusick et al. 2014), and predicting forest-fire propagation (Lopes et al. 2002). In particular, identifying wind-turbine locations and designing wind-resistant structures require the accurate prediction of the wind fields, since the former is associated with the wind power that is proportional to the cube of the wind speed, while the latter involves the square of the wind speed (e.g., Şen 2003; Baker 2010). Therefore, observing and accurately simulating the mean and turbulent flow in the lower atmosphere over complex terrain remains an important subject of study (e.g., Ma and Liu 2017; Hancock et al. 2018; DeLeon et al. 2018).

In the experiments described by Ishihara and Hibi (1998) and Ishihara et al. (1999), two types of upwind atmospheric-boundary-layer (ABL) flows were modelled, and the flow over the hills was examined. The scaled roughness lengths of the modelled upwind ABL flow are 0.3 m and 0.01 m, corresponding to suburban or wooded countryside and flat grassy plains, respectively. While these experimental studies provide a fundamental understanding of the flow over a hill, full three-dimensional (3D) views of the mean and turbulent flow fields over a 3D hill are still lacking, given that most studies focus primarily on illustrating the flow features in a vertical cross-section through the hilltop. In addition, studies rarely take into account the full suite of important parameters, including the spatial correlations of velocities for the estimation of the integral length scale and identification of the coherent turbulent structures, as well as the skewness and kurtosis for the estimation of the peak velocities.

The case with a smooth surface of 0.01-m roughness length in the experiment of Ishihara et al. (1999) is modelled here in consideration of the northern part of China where many hills are smooth and lacking tree cover, and are thus rich in wind energy. A detailed examination of the flow characteristics is, therefore, meaningful for the design of wind turbines in this region. However, it should be pointed out that ABL flow over topography can be affected significantly by the surface roughness. For example, the flow over a rougher surface may be more likely to separate (e.g. Gong et al. 1996), and details of the separation line will depend on the approaching flow profile. With an aerodynamically smooth surface, the Reynolds number may also affect separation (Zilker et al. 1977).

The mean and turbulent flow fields and coherent turbulent structures over an isolated 3D hill are simulated and analyzed here with large-eddy simulations (LES) after validation against wind-tunnel data. To construct the turbulent flow fields, the following variables are selected to describe the turbulent statistics: (a) mean and fluctuations of pressure and velocity, (b) turbulence kinetic energy (TKE), (c) the vertical momentum flux uw, (d) the vertical momentum flux in the second quadrant uw_{II} caused by ejection motion, (e) the vertical momentum flux in the fourth quadrant uw_{IV} caused by sweeping motion, (f) the ratio between uw_{IV} and uw_{II}, $Q_{uw} = uw_{\mathrm{IV}}/uw_{\mathrm{II}}$, enabling quantification of the overall relative contribution of the ejection and sweeping eddy motions to the mean momentum flux, (g) correlations between the streamwise and vertical velocities R_{uw} representing the efficiency of turbulence for momentum transport, (h) the skewness Sk_{u_i} providing information about the symmetry of the probability distribution of the velocity fluctuations u_i around the mean value, (i) the kurtosis Ku_{u_i} providing information about the peakedness of the probability distribution of

velocity fluctuations u_i, (j) the two-point spatial correlations of the velocity components $R_{u_i u_i}$ providing information about the turbulence length scale, and (k) the Q-criterion. This criterion enables quantification of the relative amplitude of the rotation rates and the strain rate of the flow for identification of vortex cores, which are examined on three surfaces, including the vertical cross-section across the hilltop, the surfaces at vertical distances of $0.25h$ and $1.25h$ from the ground, h being the hill height. A 3D view of the flow fields using the Q-criterion is also provided, the main objective being to obtain a full view of the flow fields and coherent structures over an isolated 3D hill.

2 Computational Details

2.1 Governing Equations

In the LES strategy, large eddies are explicitly resolved, while the small eddies are parametrized by subgrid-scale (SGS) models. The governing equations are usually obtained by filtering the time-dependent Navier–Stokes equations in Cartesian coordinates (x, y, z),

$$\frac{\partial \rho \tilde{u}_i}{\partial x_i} = 0, \tag{1}$$

$$\frac{\partial \rho \tilde{u}_i}{\partial t} + \frac{\partial \rho \tilde{u}_i \tilde{u}_j}{\partial x_j} = \frac{\partial}{\partial x_j}\left(\mu \frac{\partial \tilde{u}_i}{\partial x_j}\right) - \frac{\partial \tilde{p}}{\partial x_i} - \frac{\partial \tau_{ij}}{\partial x_j}, \tag{2}$$

where $\tilde{u}_i$ and $\tilde{p}$ are the filtered velocity and pressure, respectively, μ is the viscosity, ρ is the density, and τ_{ij} is the SGS stress. To close the equations for the filtered velocities, a model for the anisotropic residual stress tensor τ_{ij} is needed, which is modelled as

$$\tau_{ij} = -2\mu_t \tilde{S}_{ij} + \frac{1}{3}\tau_{kk}\delta_{ij}, \tag{3}$$

$$\tilde{S}_{ij} = \frac{1}{2}\left(\frac{\partial \tilde{u}_i}{\partial x_j} + \frac{\partial \tilde{u}_j}{\partial x_i}\right), \tag{4}$$

where μ_t denotes the SGS turbulent viscosity, $\tilde{S}_{ij}$ the rate-of-strain tensor for the resolved scale, and δ_{ij} is the Kronecker delta. The Smagorinsky–Lilly model is used to parametrize the SGS turbulent viscosity (Ferziger and Peric 2002) as

$$\mu_t = \rho L_s^2 \left|\tilde{S}\right| = \rho L_s^2 \sqrt{2\tilde{S}_{ij}\tilde{S}_{ij}}, \tag{5}$$

$$L_s = \min\left(\kappa d, C_s \Lambda^{1/3}\right), \tag{6}$$

where L_s denotes the SGS mixing length, κ is the von Kármán constant (=0.42), d is the distance to the closest wall, and Λ is the volume of a computational cell. Here, C_s is the Smagorinsky constant, which is set to a value of 0.1 following Iizuka and Kondo (2006).

When the cells are in the viscous sublayer, the shear stresses are obtained from the viscous stress–strain relation

$$\frac{\tilde{u}}{u_*} = \frac{\rho u_* \delta_n}{\mu}, \tag{7}$$

where u_* is the friction velocity, and δ_n is the distance between the centre of the cell and the wall. If the mesh cannot resolve the viscous sublayer, it is assumed that the centroids of

the cells fall within the logarithmic region of the boundary layer, and the law-of-the-wall is employed as

$$\frac{\tilde{u}}{u_*} = \frac{1}{\kappa} \ln \Theta \left(\frac{\rho u_* z}{\mu} \right), \tag{8}$$

where the constant $\Theta = 9.793$.

2.2 Method for Simulating Roughness Elements

The canopy model has been widely applied to simulate roughness elements by adding an appropriate source term $f_{\tilde{u},i}$ to the momentum equation,

$$\frac{\partial \rho \tilde{u}_i}{\partial t} + \frac{\partial \rho \tilde{u}_i \tilde{u}_j}{\partial x_j} = \frac{\partial}{\partial x_j} \left(\mu \frac{\partial \tilde{u}_i}{\partial x_j} \right) - \frac{\partial \tilde{p}}{\partial x_i} - \frac{\partial \tau_{ij}}{\partial x_j} + f_{\tilde{u},i}, \tag{9}$$

$$f_{\tilde{u},i} = -\frac{1}{2} p C_f \frac{\gamma_0}{l_0} \tilde{u}_{\text{mag}} \tilde{u}_i, \tag{10}$$

where $C_f = C_{D,\tilde{u}_i} / \left(1 - \gamma_0^2\right)$, with the drag coefficient $C_{D,\tilde{u}_i} = 0.4$ following Kaimal and Finnigan (1994). Here, $\gamma_0 = \Lambda_0 / \Lambda_{\text{grid}}$ is the volume-occupancy rate, Λ_0 is the volume occupied by the obstacle, Λ_{grid} is the volume of the grid containing the obstacle, $l_0 = \Lambda_0 / A_0$ is the representative length, and A_0 is the frontal area of the single roughness element. For the grids within the solid-roughness elements, $\Lambda_0 = \Lambda_{\text{grid}}$, and, therefore, the volume-occupancy rate $\gamma_0 = 1$ for these grids, and hence $C_f = \infty$, so that velocities in the same volumes of the solid-roughness elements are close to zero to reproduce the solid drag effects on the fluid. In the numerical simulations using the canopy model introduced above, the volumes occupied by the roughness elements can be defined using certain functions without explicitly building the geometries in the mesh-generation procedure. For the grid cells located in the volumes determined by the functions, the drag-force terms $f_{\tilde{u},i}$ given in Eq. 8 are added to the momentum equations to represent the effects of the solid elements, which can be carried out by user-defined functions in the ANSYS Fluent version 14.0 software (2014). For different arrangements of the roughness elements, the geometry of the computational domain and the mesh system do not need to be rebuilt; rather, we must simply modify the functions determining the roughness elements so as to avoid the repeated tasks.

2.3 Computational Domain

To evaluate the performance of our simulations, a neutrally-stratified ABL experiment in a wind tunnel (Ishihara et al. 1999) was simulated (Fig. 1). The return wind tunnel had a test Section 1.1-m wide, 0.9-m high, and 7-m long, containing three rows of cubic roughness elements of height 60 mm, followed by 20 mm and 10 mm covering 1.2 m of the test-section floor (0.4 m each), corresponding to areal densities of 25%, 2.8%, and 0.7%, respectively (Fig. 1b). The parameters in our numerical model are the same as for the wind-tunnel experiment except the width of the wind tunnel and the upstream necking zone (Fig. 1a). For both of the experiment and the model, the origin is 3.4-m downstream from the roughness blocks, corresponding to the centre of the 3D hill. Mason and Thomson (1987) recommend a width of approximately twice the boundary-layer depth for reproducing the largest eddies in the ABL. Taking into account the convenience in generating the roughness elements, we set a value of 1.8 times the boundary-layer thickness (i.e., 0.66 m). An upstream buffer zone (i.e., 2-m long) was appended to minimize any perturbations from the effect of the inlet condi-

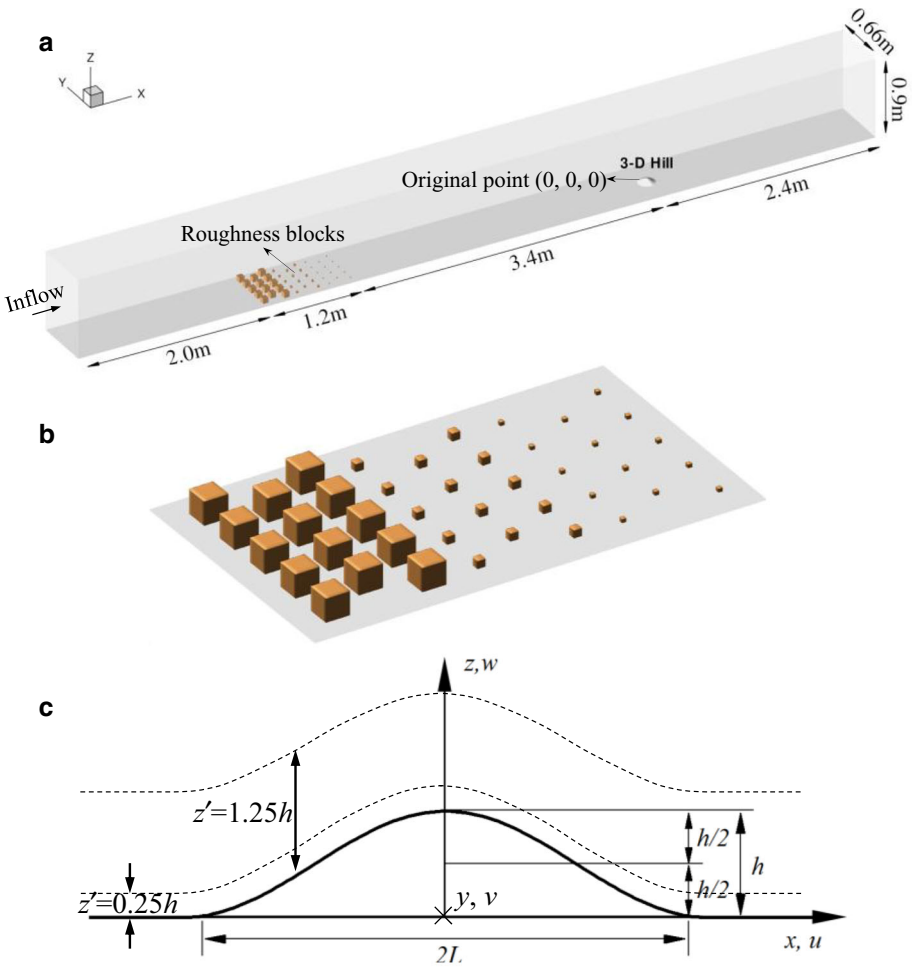

Fig. 1 Configurations of the computational domain: **a** geometry of the numerical wind tunnel, **b** the arrangement of the roughness elements, **c** coordinates and notations used here. The dashed lines in Fig. 1c denote the surfaces with vertical distances of $0.25h$ and $1.25h$ from the surface

tions on the turbulence-generation region. The outlet of the numerical model was set 2.4 m downstream from the origin, which is 60 times as large as the height of the simulated 3D hill, to avoid any influence from the outlet on the region of interest. The 3D hill is defined by the functions $z_s(x, y) = h\cos^2\pi(x^2+y^2)^{1/2}/2L$ for $(x^2+y^2)^{1/2} < L$, and $z_s(x, y) = 0$ for $(x^2+y^2)^{1/2} > L$, where x, y, and z are the streamwise, spanwise, and vertical directions, respectively, and $h = 40$ mm and $L = 100$ mm for a maximum slope of $\approx 32°$. Figure 1c shows the side view of the 3D hill and the coordinate system. A second vertical coordinate $z' = z - z_s(x, y)$ is also used to denote the height above the local surface.

2.4 Grid System

The grid-nesting procedure illustrated in Fig. 2a, where the dark grey area shows the fine-grid region, minimizes the impact of the lateral boundaries and simulates the flow over an isolated hill within an acceptable computational time. The fine-grid domain covers the range $(L_x, L_y, L_z) = (30h, 5h, 5h)$ in the x, y, and z directions, respectively. Both the upstream and downstream fine-grid regions are of length $15h$, which is large enough to absorb the perturbations from the change of the grid at the beginning and end of the fine-grid domain according to the flow visualization presented below. Within the fine grid, the horizontal grid shape is square, with horizontal resolutions of 5.65 mm, 4 mm, 2.8 mm, and 2 mm having been examined. Since the horizontal resolutions of 2.8 mm and 2 mm lead to almost the same results, the 2-mm resolution is used for the fine grid. The light grey area in Fig. 2a between the coarse-grid region in white and fine-grid region in dark grey denotes the buffer zone, which increases from 2 mm at the boundary of the fine-grid region to 10 mm at the inner boundary of the coarse-grid region. The horizontal grid shape within the buffer zone is quadrilateral, with a growth factor of 1.2. In the rough-grid region, the horizontal grid shape is square, and a uniform grid size of 10 mm is applied. The choice of the size and resolution of our nested domains results from a compromise between constraints related to the available computational time and the sufficient domain size to represent the largest eddies and fine enough to represent the smallest eddies of interest. In Fig. 2a, the white dashed circle indicates the area covered by the 3D hill. In the vertical direction, a regular terrain-following mesh is adopted, which in the first-layer grid is $0.005h$, and the maximum growth ratio is 1.15. The value of $z_+ = zu_*/\nu$ at the surface of the target region varies between 0.5 and 1, while the total grid number is 2.4×10^7. Figure 2b shows the vertical cross-section through the origin of the 3D hill.

2.5 Boundary Conditions

A stress-free boundary condition is used at the top of the domain and the spanwise sides, a uniform flow with a constant speed of 5.4 m s^{-1} in time is set at the inlet, and the outlet boundary has zero normal gradients of pressure and velocities. The non-slip condition is applied at the bottom surface with the wall functions; settings for all boundary conditions are listed in Table 1.

2.6 Solution Scheme and Procedure

The finite-volume method is used for the simulations in which all the variables are distributed in a non-staggered, cell-centred mesh system. Similar to the finite-difference or finite-element methods, variables are evaluated discretely on a meshed geometry in the finite-volume method. The finite volume refers to the small volume surrounding each node point on a mesh, enabling the conversion of divergence terms within the volume to surface integrals using the divergence theorem, and these terms are then evaluated as fluxes at the surfaces of each finite volume. Because the flux entering a given volume is identical to that leaving the adjacent volume, the finite-volume method is conservative, which is its greatest advantage. The second-order central-difference scheme is used for the convective and viscous terms,

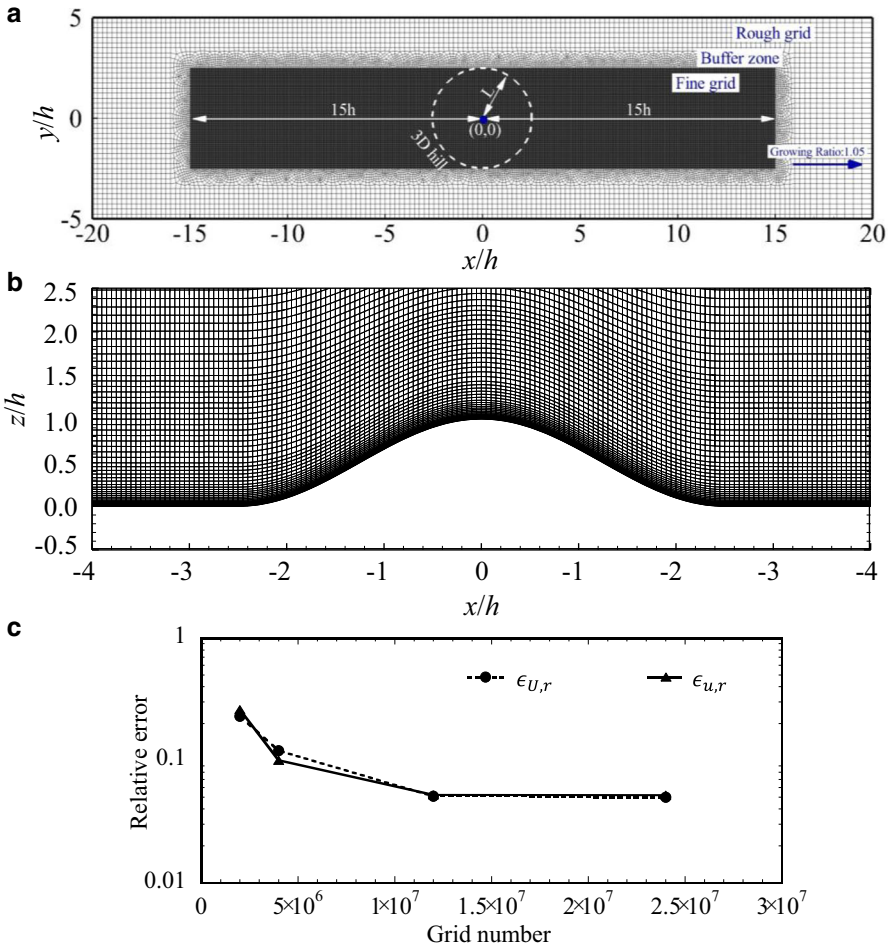

Fig. 2 Grid distributions of the model: **a** schematic showing the locations of the coase grid, buffer zone, and fine grid of the nested domain. The white, dashed circle denotes the 3D hill. The x- and y- axes are normalized by the height h. **b** Distributions of the mesh on the vertical cross-section at the centre of the 3D hill. The x- and z- axes are normalized by the height h. **c** Relative errors of the mean streamwise velocity component $\epsilon_{U,r}$ and r.m.s. of the streamwise velocity component $\epsilon_{u,r}$ versus grid number

and the second-order implicit scheme is employed for the unsteady term (Ferziger and Peric 2002),

$$\left(\frac{\mathrm{d}\phi}{\mathrm{d}t}\right)_n = \frac{3\phi^n - 4\phi^{n-1} + \phi^{n-2}}{2\Delta t_n}, \quad \Delta t_n = t - t_{n-1} = t_{n-1} - t_{n-2}, \tag{11}$$

where n and $n-1$ denote the new and old times, respectively, and ϕ is an arbitrary variable. The timestep $\Delta t = 0.0001$ s, which in the convective time scale $\Delta t^* = \Delta t U_h/h = 0.0109$, where $U_h = 4.37$ m s^{-1} is the mean wind speed at the point ($x = 0$, $y = 0$, $z = h$) when the ground is flat, giving a Reynolds number at the hill height $Re = U_h h/\upsilon = 1.16 \times 10^4$. The method consists of linearizing the non-linear equations and implementation into a matrix solution, and the predicted conjugate-gradient method is applied to solve the linearized equations along with the algebraic multi-grid approach. The Courant–Friedrichs–Lewy number (Courant et al. 1928) expressed as $C = \Delta t \Sigma \tilde{u}_i/\Delta x_i$, where $\tilde{u}_i$ is the velocity, and Δx_i is

Table 1 Settings of the boundary conditions

Locations	Boundary type	Expression
Outlet of the domain	Outflow	$\partial\tilde{u}_i/\partial n = 0$, $\partial\tilde{p}/\partial n = 0$
Lateral sides of the domain	Symmetry	$\partial\tilde{p}/\partial n = 0$, $\partial\tilde{u}/\partial n = 0$, $\partial\tilde{w}/\partial n = 0$, $\tilde{v} = 0$
Top of the domain	Symmetry	$\partial\tilde{p}/\partial n = 0$, $\partial\tilde{u}/\partial n = 0$, $\partial\tilde{v}/\partial n = 0$, $\tilde{w} = 0$
Inlet of the domain	Velocity inlet	$\tilde{v} = 5.4\ \mathrm{m\ s^{-1}}$, $\partial\tilde{u}/\partial n = 0$, $\partial\tilde{w}/\partial n = 0$, $\partial p/\partial n = 0$
Ground	Non-slip wall	$\partial\tilde{p}/\partial n = 0$, $\tilde{u}_i = 0$

Table 2 Numerical schemes

Time-discretization scheme	Second-order implicit scheme	*Cs* number	0.1
Space-discretization scheme	Finite-volume method second-order central-difference scheme	SGS model	Smagorinsky–Lilly
Non-dimensional time step size: $\Delta U_h h$	0.0109	CFL number: $\Delta t \Sigma u_i/\Delta x_i$	<2
Reynolds number $Re = U_h h/\upsilon$	1.16×10^4	Velocity–pressure decoupling method	SIMPLE algorithm
Turbulence model	LES	Software	ANSYS Fluent 14.0
Time for statistics	20 s	Solution of the linearized equations	Preconditioned conjugate gradient + algebraic multigrid

the grid size, is limited to $C_{\max} = 2$ in the whole computational domain. The semi-implicit pressure-linked-equations algorithm (also known as the SIMPLE algorithm), which was introduced by Ferziger and Peric (2002), is used to solve the discretized equations. Relaxation factors, which are employed to promote the stability of the process, take values of 0.3 and 0.7 for the pressure and momentum equations, respectively. The commercial software ANSYS Fluent 14.0 (2014) is used for the calculations.

As the initial transient effects are found to disappear after 10 s, data sampling begins at 10 s and lasts for 20 s. A stationary condition for time sampling can be achieved by evaluating the relative errors in the U velocity component at the point ($x = L$, $y = 0$, $z = h$), which becomes less than 1% when the data from 10–30 s are sampled. Consequently, the filtered velocity components in the simulations can be decomposed into $\tilde{u}_i = U_i + u_i^{'}$, where $U_i(U, V, W)$ denote the time-averaged velocity components in the x_i (x, y, z) directions, and $u_i^{'}$ (u', v', w') are the corresponding deviations from the time-averaged velocity. The root-mean square (r.m.s.) of $u_i^{'}$ is denoted as u_i as shorthand for the commonly-used notation σ_{u_i}. The simulations were performed in parallel (four PCs, Intel core i9-7980XE processors, 18 cores, 64 GB memory), costing 1308h for a 30-s simulation. Table 2 summarizes the numerical schemes adopted here.

Table 3 Case settings and computational resources

Cases	Horizontal grid size (mm)	Grid number (N)	Computational time (h)	CPU	Memory
1	5.65	2×10^6	152	Four PCs (Intel i9-7980XE, 18 cores) in parallel	64 GB
2	4	4×10^6	396		
3	2.8	1.2×10^7	689		
4	2	2.4×10^7	1308		

2.7 Grid Independency and Validations

Four grid systems (cases 1–4) with increasing horizontal resolution from 5.65 to 2 mm (see Table 3) are deployed to test the grid convergence, with the coarse grid-number increment twice that of the finer mesh. Except for the grid density, the other settings, such as the solution schemes, boundary conditions, and initial values, are all set the same. The mean streamwise velocity component U and r.m.s. of u' along the line ($x = L$, $y = 0$, $z = [0, 4h]$) are then compared for different mesh densities.

To clearly show the grid independency, the relative errors as a function of the grid number are also analyzed. First, the errors (ϵ_U for U and ϵ_u for u) are defined as the integrals of the absolute difference between the simulations and the experimental data,

$$\epsilon_U = \int_{0.0h}^{4h} |U_e(z) - U(z)| dz \tag{12a}$$

$$\epsilon_u = \int_{0.0h}^{4h} |u_e(z) - u(z)| dz, \tag{12b}$$

where the subscript e indicates the experimental data, and are then normalized by the integrated experimental data to determine the relative errors defined by

$$\epsilon_{U,r} = \frac{\epsilon_U}{\int_{0.0r}^{10r} U_e(z) dz} \tag{13a}$$

$$\epsilon_{u,r} = \frac{\epsilon_u}{\int_{0.0r}^{10r} u_e(z) dz}. \tag{13b}$$

Figure 2c shows that, as the grid number increases, the relative errors monotonically decrease, but are almost a constant 5.2% for the cases 3 and 4, which is sufficiently accurate for applications. Therefore, we conclude that a grid with a total of 24 million nodes reaches grid independency. For this grid system, the maximum SGS viscosity is about 0.7×10^{-5}, which is about half of the viscosity of the air. Both the values of U and W as well as the r.m.s. of u_i' show satisfactory agreement with experiments, as illustrated in Fig. 3.

Consistent with Gong and Ibbetson (1989), the modelled results also indicate that the mean and turbulent flow over a 3D hill are broadly similar with those over a two-dimensional ridge, but the perturbation amplitudes for the 3D hill are largely reduced compared with those for the two-dimensional ridge. In another experimental study, Ishihara et al. (2001) compared the flow fields over a two-dimensional ridge with those over a 3D hill, identifying opened

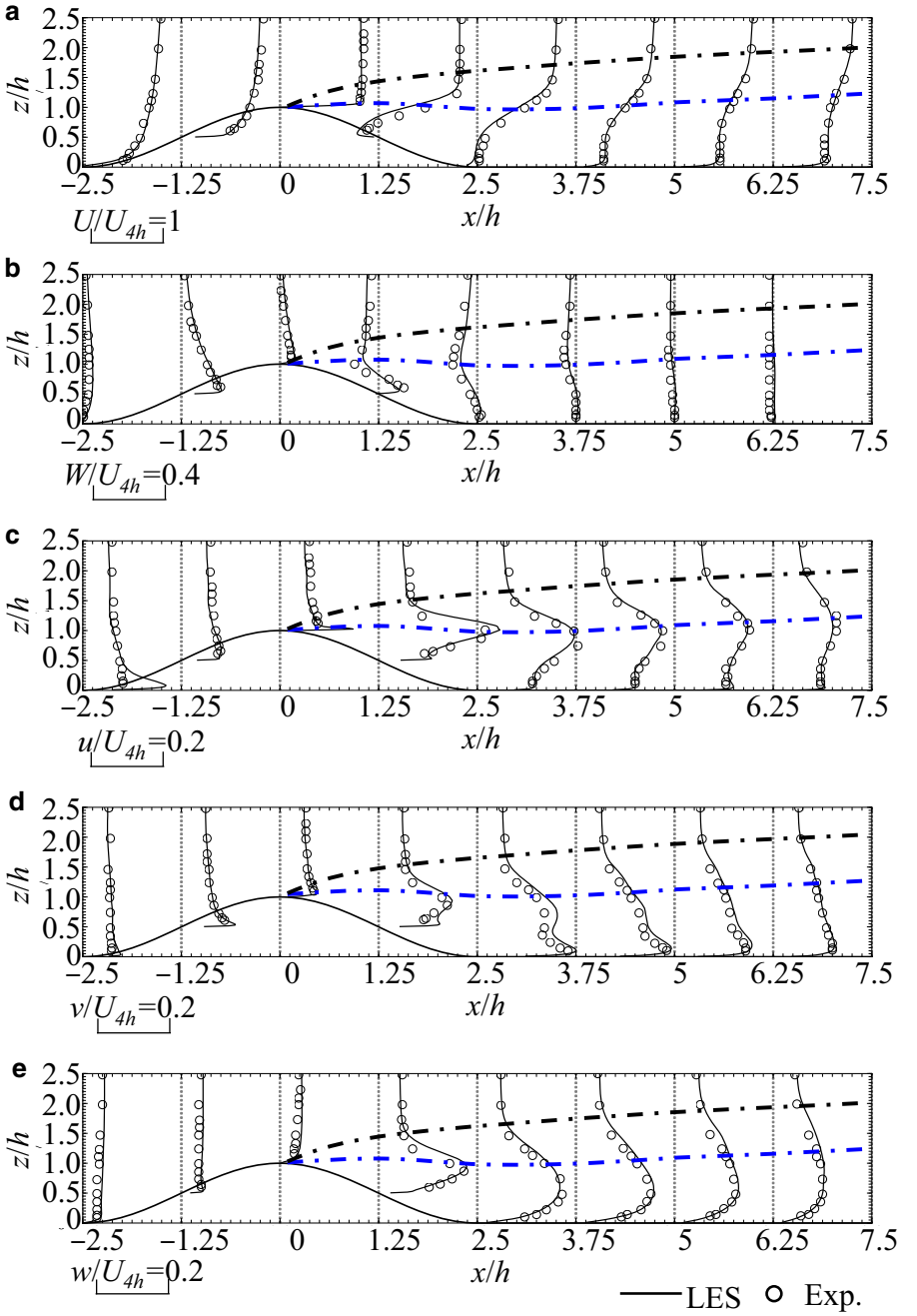

Fig. 3 Profiles of the mean and fluctuating velocity components on the vertical cross-section at $y = 0$: mean of the **a** streamwise, and **b** vertical velocity components, and r.m.s. of the **c** streamwise c, **d** spanwise, and **e** vertical velocity components. The black and blue dash–dot lines are the wake depth and the shear layer, respectively. The x- and z-axes are normalized by the height h. The red points with $z' = 1.25h$ denote the reference points for the calculations of the space correlations in Sect. 3. The velocities U_i and u_i are normalized by the wind speed U_{4h}

streamlines in the wake of the 3D hill, but closed ones in the wake of the two-dimensional ridge. Whereas the statistics of the flow in the wake of a two-dimensional ridge are two dimensional, 3D statistics are found in the wake of 3D hill, and hence are more complex. Clarifying the 3D characteristics of the flow in the wake is, therefore, one of the motivations of our study.

3 Results

In the following three sections, the simulated results across the vertical cross-section at the hilltop (i.e., $y = 0$), the surface $0.25h$ above the ground (i.e., $z' = 0.25h$), and the surface $1.25h$ above the ground (i.e., $z' = 1.25h$), are analyzed to examine features of the 3D flow.

3.1 Upwind Flow Properties

That the mean and turbulence profiles of the upwind flow influence the flow separation and patterns has been pointed out by Cao and Tamura (2006), and Liu et al. (2016) suggest it is meaningful to first examine whether the upwind ABL has been reproduced well, where Fig. 4a compares the simulated upwind mean velocity profiles with the experiments in Ishihara et al. (1999). The vertical coordinate is normalized by the height h and the mean velocities are normalized by $U_{4h} = 5.2$ m s^{-1}, which is the mean wind speed at the height of $4h$ when the terrain is flat. Figure 4b shows that the generated upwind turbulence statistics are in satisfactory agreement with the experimental data. However, the maximum value of u, which occurs close to the bottom of the wind tunnel, is considerably larger in the simulation than in the experiments, which is consistent with previous simulations (e.g., Iizuka and Kondo 2004; Tamura et al. 2007a, b), and results from the difference of the conditions on the bottom in experiments and simulations. While the bottom of the numerical wind tunnel is absolutely smooth, the surface of the actual wind tunnel is not completely smooth, which disturbs the flow near the surface. However, the spanwise and vertical components of turbulence in the simulation agree well with the experiments. The vertical profiles of mean velocities, as well as three components of fluctuations at the locations of $x = -L$, $y = 0$ and $x = L$, $y = 0$ are also extracted and compared with those at $x = 0$, $y = 0$, illustrating good agreement (not shown), and implying a fully-developed and stable boundary layer.

3.2 Centreline Flow Characteristics

Figure 5 shows the normalized parameters P, U_i, p, u_i, and TKE through the vertical cross-section at $y = 0$. The white and yellow dash–dot lines represent the upper limit of the wake region and the connection of the u peaks, respectively. The maximum SGS variance is located just behind the summit, which represents only 4% of the resolved variance. Following Kaimal and Finnigan (1994), the wake depth is defined as the height at which the value of U is equal to the value upstream of the hill at the same height. Here, the wake depth h_w, which is calculated as $|U_{down}(h_w) - U_{up}(h_w)|/U_{up}(h_w) < 0.01$, with U_{down} and U_{up} the values of U downstream and upstream of the hill, respectively, increases quickly from $x = 0$ to $x = 5h$, followed by a gentle increase. Additionally, the connection of the u peaks indicates the strongest turbulence region or the central part of the shear layer, whose height slightly decreases from the domain top to $x = 2.5h$, and then increases at a rate larger than that of the wake depth. The region

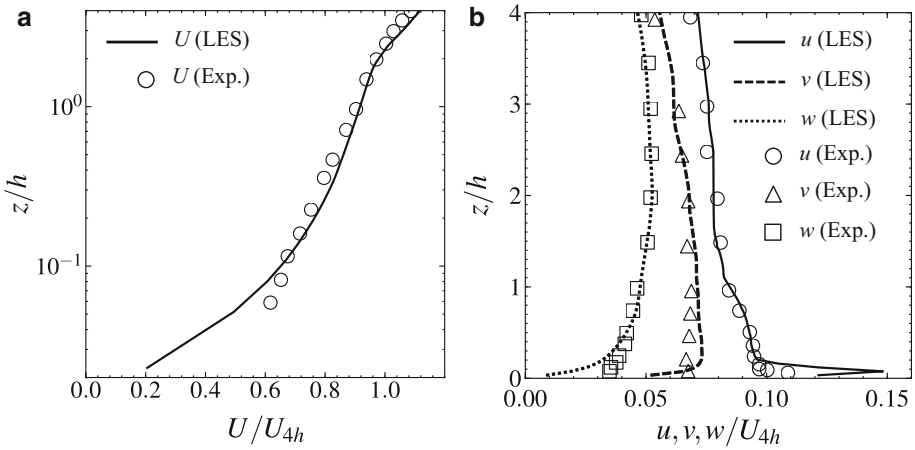

Fig. 4 Profiles of the **a** mean streamwise velocity component, and **b** turbulence fluctuating velocity components of the upwind flow according to experiments (markers) and simulations (lines)

enclosed by the white and yellow dash–dot lines roughly implies the shear-layer region narrowing on its way downstream of the hill.

Approaching the hilltop from $x = -5h$, the value of U decreases on the upwind side of the hill due to the obstruction of the hill (Fig. 5b), which is accompanied by an increase in the value of P (Fig. 5a) and a positive value of W (Fig. 5c). In fact, the flow reacts as if the hill and its separation region are two single obstacles. In order to identify the separation region, the locations of zero streamwise velocity are delimited by the thick, black dotted lines in Fig. 5 from $x = 0.9h$ to $x = 2.5h$. These results are almost the same as the experimental data reported in Ishihara et al. (1999). In this recirculation region, the global minimum pressure $P_{\min} = -0.4$ occurs at $x = h$, $z' = 0.3h$, and, on the top of this region, the maximum pressure fluctuation is found associated with the streamwise velocity component and the large shear stress there (Fig. 5d, e). The v component shows two peaks in the vertical direction at $x = 2.5h$ (Fig. 5f), with the peak closer to the ground having much larger fluctuations than the peak above. The elevated v peak occurs at the same location as that of the u peak, indicating that, apart from the separation of the flow at the hilltop, there should be another factor contributing to the magnitude of the v component. Just downstream of the recirculation, the value of w reaches its maximum because of the unsteady flapping of the flow observed in vorticity animations at $y = 0$ (Fig. 5g). It is interesting that there is a reduction in the magnitude of w and an increase in the value of u over the hilltop consistent with the rapid-distortion theory of Hunt and Carruthers (1990). The eddies of the upwind flow are stretched by the mean flow at the summit of the hill, resulting in their elongation in the streamwise direction, but flattening in the vertical direction, as shown in Fig. 16 (below).

Comparing the values of u, v and w shows that the u component contributes primarily to the TKE (Fig. 6a), and, therefore, both the k and u peaks have the same location. Also shown in Fig. 6 is the total vertical momentum flux $uw = \langle u'w' \rangle$, where $\langle\,\rangle$ indicates a time average, the vertical momentum flux in the second quadrant uw_{II} (Fig. 6c) caused by ejections, the vertical momentum flux in the fourth quadrant uw_{IV} (Fig. 6d) caused by sweeping motions, the ratio between uw_{IV} and uw_{II}, $Q_{uw} = uw_{\mathrm{IV}}/uw_{\mathrm{II}}$ (Fig. 6e), as well as the correlation coefficient between the u and w components $R_{uw} = \langle u'w' \rangle / uw$, representing the efficiency of turbulence for momentum transport. These parameters quantify the overall relative contributions of

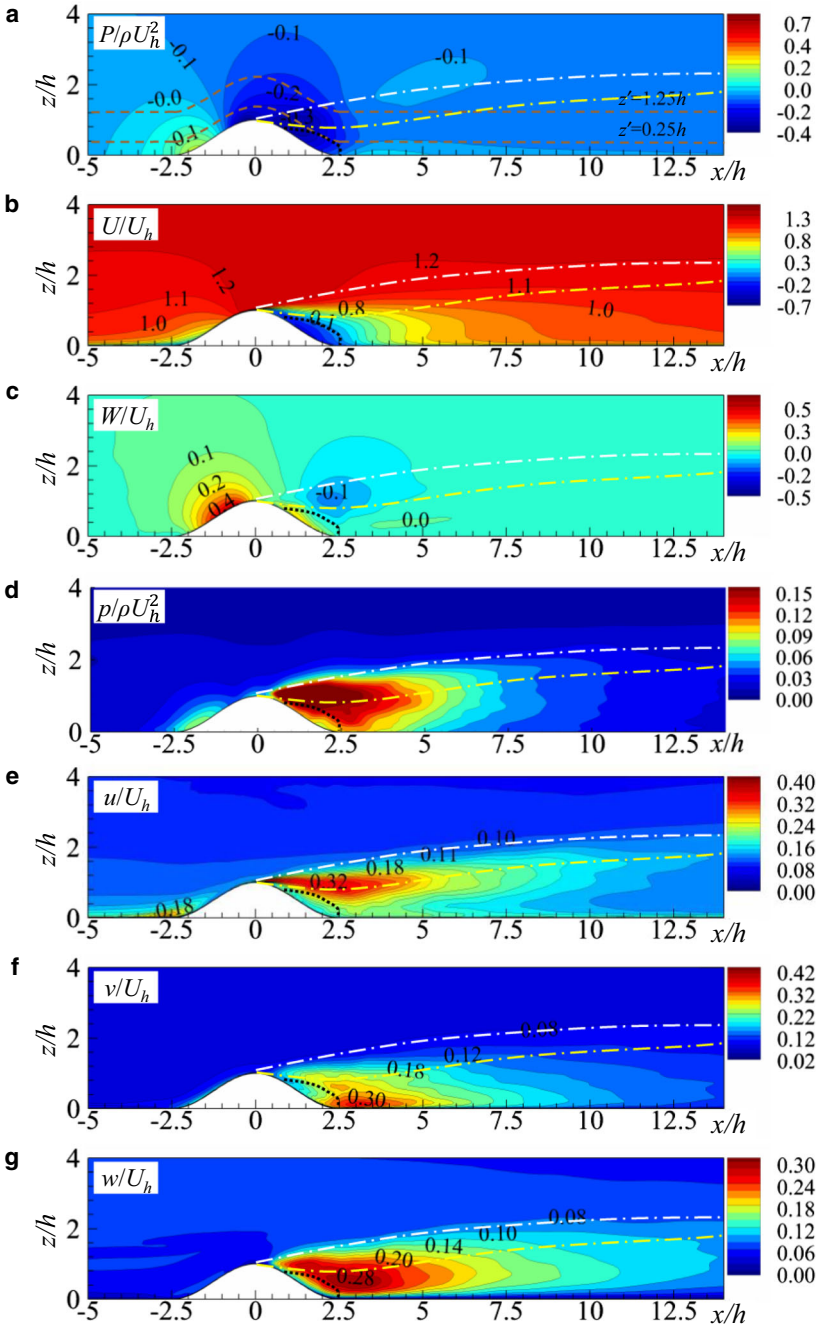

Fig. 5 Vertical cross-sections through $y = 0$ of the mean **a** pressure, and **b** streamwise and **c** vertical velocity components, and the r.m.s. of **d** pressure, and **e** streamwise, **f** spanwise, and **g** vertical velocity components. The brown, thin dashed lines in **a** are the locations of the flow fields discussed in Sects. 3.2 and 3.3. The white and yellow dash–dot lines denote the boundaries of the wake depth and shear layer, respectively. The thick, black dashed lines show the boundary of the separation bubble with zero mean streamwise velocity. The x- and z-axes are normalized by the height h

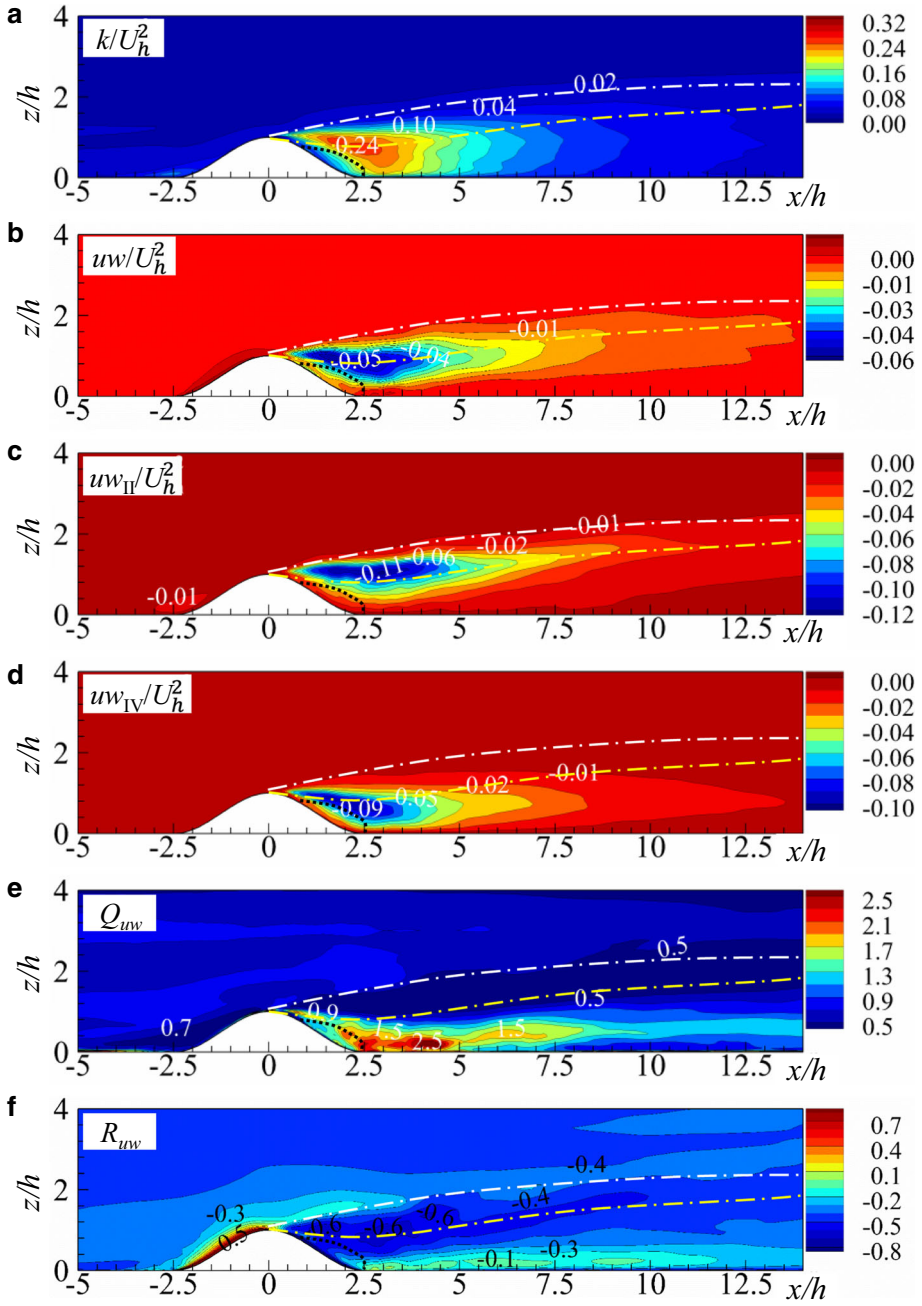

Fig. 6 Distributions of the normalized **a** TKE, **b** vertical momentum flux uw, **c** vertical momentum flux in the second quadrant, uw_{II}, **d** vertical momentum flux in the fourth quadrant, uw_{IV}, **e** ratio between the vertical momentum flux in the fourth and second quadrants, Q_{uw}, and **f** the correlation coefficient between streamwise and vertical velocity components R_{uw} through the cross-section at $y = 0$. The white and yellow dash–dot lines denote the boundaries of the wake depth and the shear layer, respectively. The black, dashed lines show the boundary of the separation bubble with zero mean streamwise velocity. The x- and z-axes are normalized by the height h

ejections and sweeps to the mean momentum flux. In most regions, the value of uw is negative, especially around the yellow dash–dot lines, with the uw peaks indicating the concentration of uw within the central part of the shear layer. Interestingly, the fluxes uw_{II} and uw_{IV} show different features. Whereas large values of uw_{II} occur in the region enclosed by the white and yellow dash–dot lines with the maximum at $x = 3h$ and $z' = h$, large uw_{IV} values occur below the central part of the shear layer, with the maximum at $x = 2.5h$ and $z' = 0.7h$, which suggests that ejections dominate sweeps above the shear layer and the inverse situation occurs below the shear layer. The ratio Q_{uw} reflects the relative contribution of ejections or sweeps to the vertical momentum flux. The contour line of $Q_{uw} = 1$ in Fig. 6e (i.e., $uw_{\mathrm{II}} = uw_{\mathrm{IV}}$) almost coincides with the yellow dash–dot line, with $Q_{uw} > 1$ below and $Q_{uw} < 1$ above. The largest values of Q_{uw} appear at the locations of unsteady or flapping flow just downstream of the recirculation. At the hilltop, the correlation coefficient R_{uw}, which is a measure of the turbulent-transport efficiency, is low (approximately -0.1), and increases rapidly to its equilibrium value (approximately -0.4) at around $x = 5h$ (Fig. 6f). Within the separation region, due to the existence of the recirculation, the values of u and w show large negative correlations with a maximum magnitude of -0.6 at the upper boundary of the bubble, and the closely packed contours of R_{uw} within the shear layer downstream of the hill are clearly observed.

The distributions of the skewness of the velocity components $\tilde{u}_i$, $Sk_{u_i} = u_i^{'3}/u_i^{'3/2}$, provide information about the symmetry of the probability distribution of the fluctuations u_i around the mean value. The kurtosis of $\tilde{u}_i$, $Ku_{u_i} = u_i^{'4}/u_i^{'2}$, which denotes the peakedness of the distribution, is shown in Fig. 7c–e. Note that the skewness of any univariate normal distribution is zero, and the kurtosis of any univariate normal distribution is 3. Further, the kurtosis should never be less than one, and is 1.8 under the uniform probability density function (p.d.f.). Note that the contour line of the streamwise velocity skewness $Sk_u = 0$ implies a symmetric p.d.f. (Fig. 7a). The large negative value of Sk_u is primarily confined within the region bounded by the yellow and white dash–dot lines, indicating that the tail on the left side of the p.d.f. is longer or wider than the right side. Because of the symmetry of the hill, the p.d.f. of the spanwise velocity component should be zero at $y = 0$ if the sampling time is long enough, and so the distributions of the spanwise velocity skewness Sk_v at $y = 0$ are not included in Fig. 7. The recirculation and the region within the wake depth are characterized by the minimum vertical velocity skewness Sk_w, and are bounded by the maximum value of Sk_w at the top of the wake, with a value of about 1.5 at $x = 10h$. The skewnesses Sk_u and Sk_w have similar distributions but opposite signs. The kurtosis for the three velocity components (Ku_u, Ku_v, Ku_w) have similar distributions, with peaks at the upper boundary of the wake, and maximum values of 15, 8, and 15 for the x, y, and z components, respectively (Fig. 7c–e), indicating very steep p.d.f. shapes. Therefore, we imagine that the tails of the p.d.f. of the velocities asymptotically approach zero more slowly than a Gaussian distribution, which, therefore, produces more outliers than the normal distribution. Away from the shear-layer region, the kurtosis recovers to almost a value of 3, indicating that the p.d.f. nearly achieves a normal distribution or the flow reaches complete mixing.

The local rotation rate of the flow can be quantified by the time-averaged enstrophy as half the square of the relative vorticity $E = \omega_i \omega_i/2$, where ω_i is the instantaneous vorticity component of the flow along x_{i}, $\omega i = \varepsilon_{ijk} \partial \tilde{u}_k / \partial x_j$. The Q-criterion, which quantifies the relative amplitude of the rotation rates and the strain rate of the flow, and thus identification of vortex cores (Shekar and Graham 2018; Tian et al. 2018), is $Q = 1/2(S_{ij}S_{ij} - \Omega_{ij}\Omega_{ij})$, where $S_{ij} = 1/2(\partial \tilde{u}_i/\partial x_j - \partial \tilde{u}_j/\partial x_i)$ and $\Omega_{ij} = 1/2(\partial \tilde{u}_i/\partial x_j + \partial \tilde{u}_j/\partial x_i)$ are the antisymmetric and symmetric components of the velocity-gradient tensor, respectively. The enstrophy starts to increase at the hilltop, and is confined within the growing layer, exhibiting a maximum

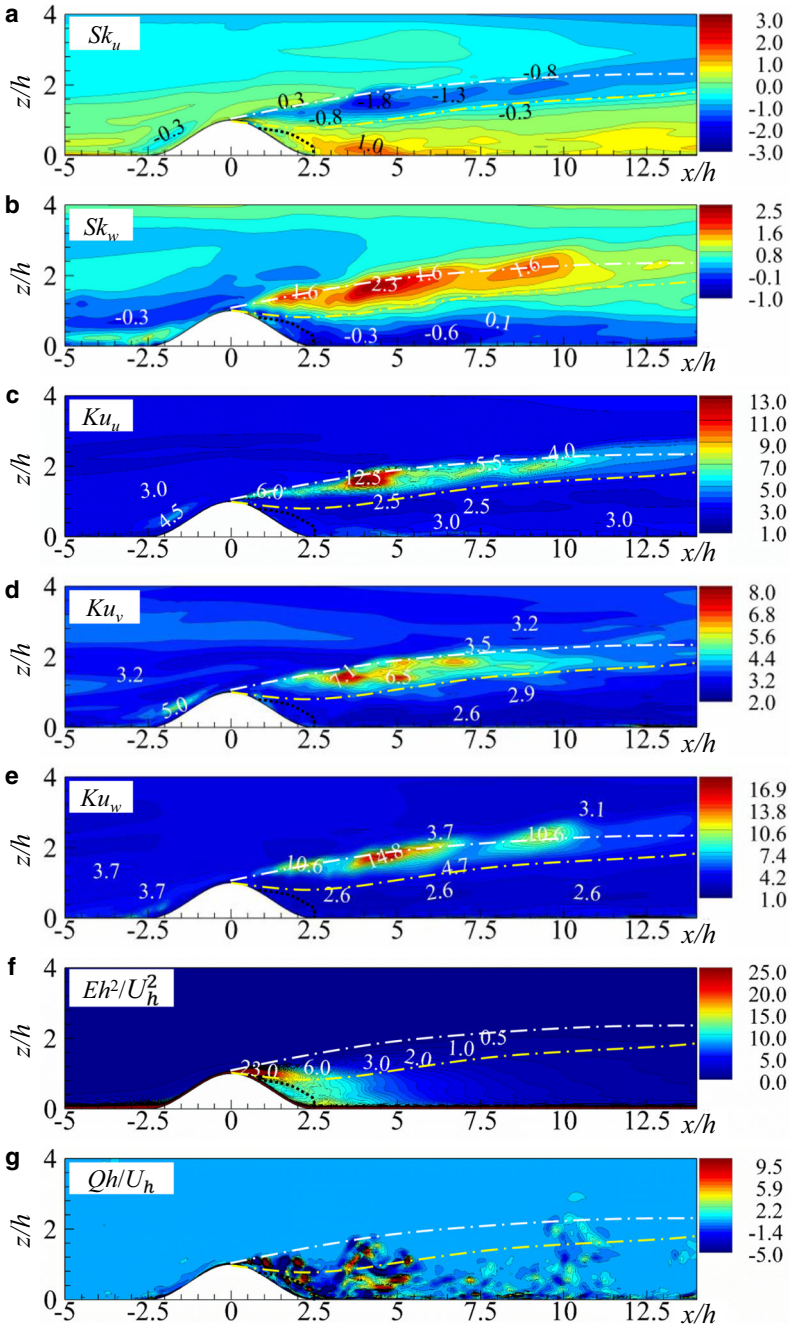

Fig. 7 Contours of skewness of a the streamwise Sk_u and **b** vertical Sk_w velocity components, and the kurtosis of the c streamwise Ku_u, **d** spanwise Ku_v, and **e** vertical Ku_w velocity components, and the **f** mean enstrophy, and **g** instantaneous Q-criterion through the vertical cross-section at $y = 0$. The white and yellow dash–dot lines denote the boundaries of the wake depth and the shear layer, respectively. The black dashed lines show the boundary of the separation bubble with zero mean streamwise velocity. The x- and z-axes are normalized by the height h

at 0.5h downstream of the hilltop (Fig. 7f). As with the value of v, two peaks in the vertical direction are also observed, with one at the centre of the shear layer, and the other close to the ground, which is an indication of different turbulence processes near the shear layer and the ground (see Sect. 3.5 for details). Large eddies are clearly identified in the Q distribution (Fig. 7g), which are generated just downstream of the hilltop and then pass through the shear-layer region, providing the concentrated skewness and kurtosis there.

Two-point space–time correlations of the velocity components provide spatial information related to the size of the main turbulent structures, and have been applied in wind-tunnel experiments (Shaw et al. 1995), field observations (Raupach et al. 1991), and LES studies (Su et al. 2000; Dupont and Brunet 2008). With respect to the four reference points (P1, P2, P3, and P4) in Fig. 3a, the zero time-lag two-point correlation coefficients are determined for the three velocity components as

$$R_{u_i u_i}(x, y, z) = \frac{u_i(x, y, z) u_i(x_{\mathrm{ref}}, y_{\mathrm{ref}}, z_{\mathrm{ref}})}{u_i(x, y, z) \cdot u_i(x_{\mathrm{ref}}, y_{\mathrm{ref}}, z_{\mathrm{ref}})}, \tag{14}$$

where $(x_{\mathrm{ref}}, y_{\mathrm{ref}}, z_{\mathrm{ref}})$ are the coordinates of the reference points (P1, P2, P3, and P4).

The contours of the correlation of the streamwise velocity, R_{uu}, for the four reference points from $x = -2.5h$–$5h$ on $y = 0$ are shown in Fig. 8a, b, g, and h. The location $z' = 1.25h$ is the reference as it is mainly within the shear-layer region as identified by the wake depth and the centre of the superimposed shear layer (Fig. 8). Well upwind from the hilltop, the coefficient R_{uu}(P1) shows a tilted, elongated elliptical region of approximately 3h in the x-direction and 2h in the z-direction (Fig. 8a). The latter feature is more obvious for the contours of R_{uu}(P2), which show a weak correlation with the wind speed in the wake region, and the correlation area of R_{uu}(P2) is more concentrated near the hilltop (Fig. 8b). This implies that strong coherent turbulent structures in the upwind flow are mostly advected above the wake area, as demonstrated by the animations of the simulated vortices (not shown). Large values of R_{uu}(P3) are mostly confined within the shear-layer region (Fig. 8g), and the size extension along the x-direction is approximately equal to the height h, which is about one-third of those in the R_{uu}(P1) and R_{uu}(P2) correlations, suggesting that very small turbulent structures exist. Consequently, we conclude that these small turbulent eddies close to the point P3 are mainly produced by shear. With increasing distance from the hilltop at the point P4, the vertical and longitudinal scales increase with the depth of the wake region (Fig. 8h).

The spanwise velocity correlations R_{vv} at points P1–4 are provided in Fig. 8c, d, l and j, illustrating clearly that the structure of the R_{vv}(P1) and R_{vv}(P2) contours (Fig. 8c, d) is similar for the coefficients R_{uu}(P1) and R_{uu}(P2) (Fig. 8a, b), with R_{vv}(P1) and R_{vv}(P2) likely more sensitive to the presence of the hill, as is evident in the remarkably tilted zones compared with the R_{uu}(P1) and R_{uu}(P2) contours. Note that the orientations of the ridges of R_{vv}(P1) and R_{vv}(P2) contours are almost parallel to the slope of the hill, with the high R_{vv}(P3) values concentrated just behind the hilltop (Fig. 8l). However, the tilt direction of the contour is opposite to that of the R_{uu}(P3) contour. The negatively correlated values below the shear layer are associated with a flow rotation, as demonstrated in Sect. 3.5, and is a feature also observed for the coefficient R_{vv}(P4) (Fig. 8j).

Correlations for the vertical velocity component R_{ww} show several different features from the coefficients R_{uu} and R_{vv} (Fig. 8e, f, k, l), with major differences that the R_{ww} zones are elongated more along the z- than the x-direction, and that R_{ww} values are negative both upstream and downstream of the points P3 and P4 (Fig. 8k, l). The strong correlation zones appear periodically (Fig. 8k), and are associated with the large vortices identified in Fig. 7g.

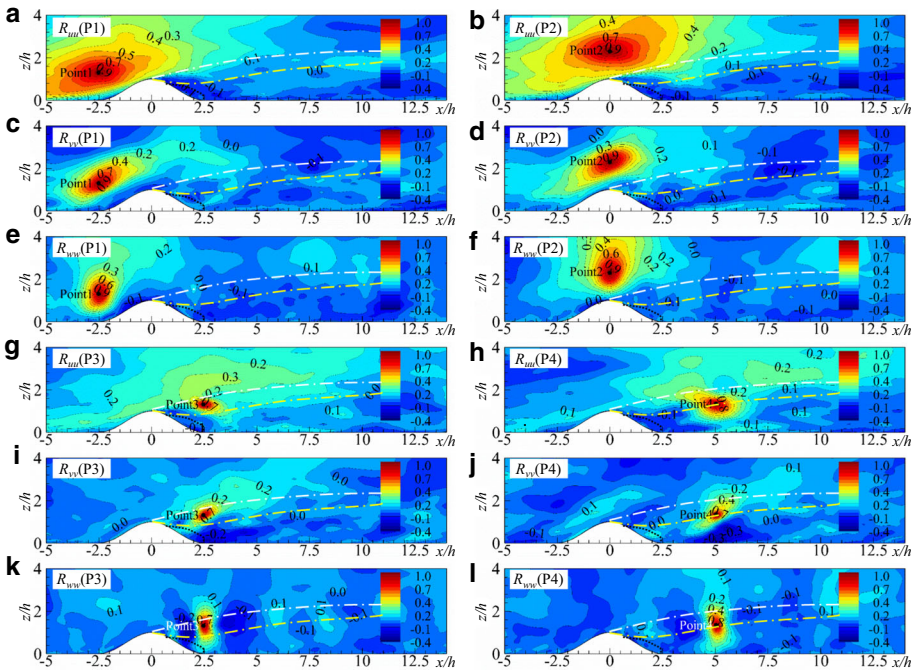

Fig. 8 Contours of the autocorrelation function for the streamwise velocity component R_{uu} computed for the reference points: **a** P1, **b** P2, **g** P3, **h** P4, spanwise velocity component R_{vv} for the reference points, **c** P1, **d** P2, **i** P3, **j** P4, and vertical velocity component R_{ww} for the reference points, **e** P1, **f** P2, **k** P3, **l** P4, on the vertical cross-section at $y = 0$. The white and yellow dash–dot lines denote the boundary of the wake depth and shear layer, respectively. The black dashed lines show the boundary of the separation bubble with zero mean streamwise velocity. The x- and z-axes are normalized by the height h

3.3 Flow Characteristics on the Plane $z' = 0.25h$

To reconstruct the 3D mean and turbulent fields over the 3D hill in detail, these quantities on the planes $z' = 0.25h$ and $z' = 1.25h$ are examined here. Taking into account the 1:1000 scale in the wind-tunnel experiment in Ishihara and Hibi (1998), the planes $z' = 0.25h$ and $z' = 1.25h$ correspond to 10 m and 50 m above ground level, respectively. Meteorological data at 10 m above ground are usually used to determine the wind-speed profiles for wind-energy applications, and a height of 50 m is generally located within the shear-layer region.

In Figs. 9, 10 and 11, the white and yellow dash–dot lines represent the boundary of the wake and the location of the centre of the shear layer, respectively, while the thick, dashed black circle denotes the 3D hill. The blockage of the hill causes positive pressure values initially (Fig. 9a), which quickly become negative at $x = -h$, resulting in flow acceleration (Fig. 9c). Due to the symmetry of the hill and the incoming flow, four regions with large values of V at the lateral sides of the hill are generated at approximately $x = -h$ and $2.5h$ and $y = \pm 1.5h$ when the flow passes around the hill (Fig. 9e). The blockage of the flow causes upwards motion upstream of the hill (positive W values), and the two downwards zones (negative W values) occur in the same locations as those with the large V values at the lateral sides of the hill (i.e., $x = 2.5h$) (Fig. 9g). As a result of these two downwards convergence flows behind the hill, the separation of the flow is generated in the region indicated by the red circle in Fig. 8.

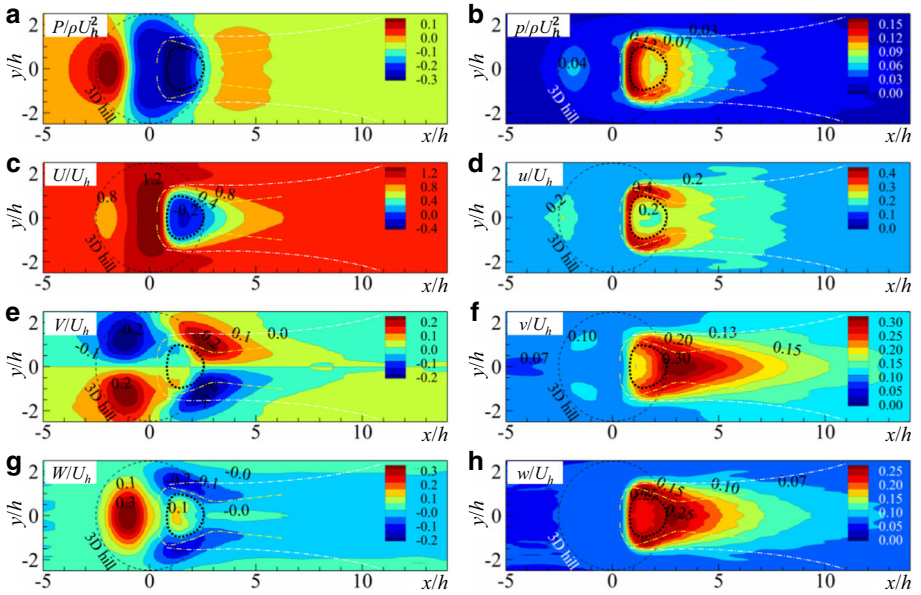

Fig. 9 Contours of the mean and fluctuating flow parameters: the **a** mean and **b** r.m.s. pressure, and the **c** mean and **d** r.m.s. streamwise, **e** mean and **f** r.m.s. spanwise, and **g** mean and **h** r.m.s. vertical velocity components on the plane $z' = 0.25h$. The white and yellow dash–dot lines denote the boundaries of the wake depth and the shear layer, respectively. The thin, black dashed circle indicates the 3D hill. The thick, black dashed line shows the boundary of the separation bubble with zero mean streamwise velocity. The x- and y-axes are normalized by the height h

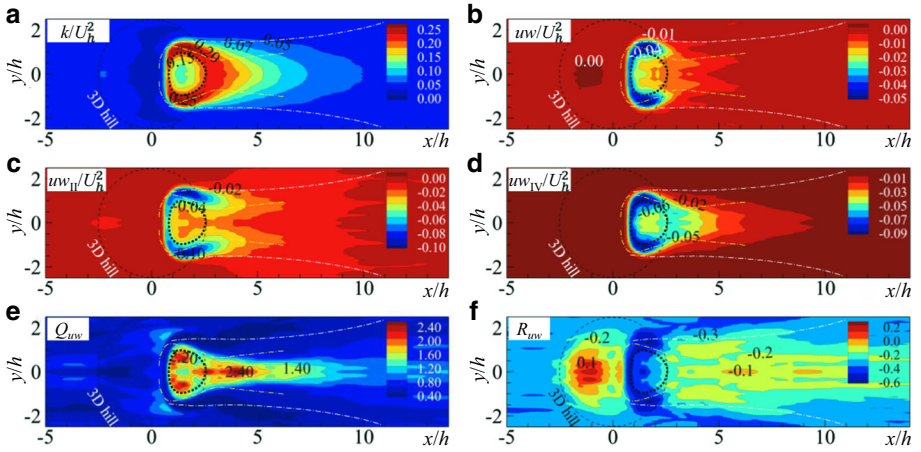

Fig. 10 Contours of the normalized **a** TKE, **b** vertical momentum flux uw, **c** vertical momentum flux in the second quadrant, uw_{II}, **d** vertical momentum flux in the fourth quadrant, uw_{IV}, **e** the ratio between the vertical momentum flux in the fourth and second quadrants Q_{uw}, and the **f** correlation coefficient between the streamwise and vertical velocity components R_{uw} on the plane $z' = 0.25h$. The white and yellow dash–dot lines denote the boundaries of the wake depth and the shear layer, respectively. The thin, black dashed circle indicates the 3D hill. The thick, black dashed lines show the boundary of the separation bubble with zero mean streamwise velocity. The x- and y-axes are normalized by the height h

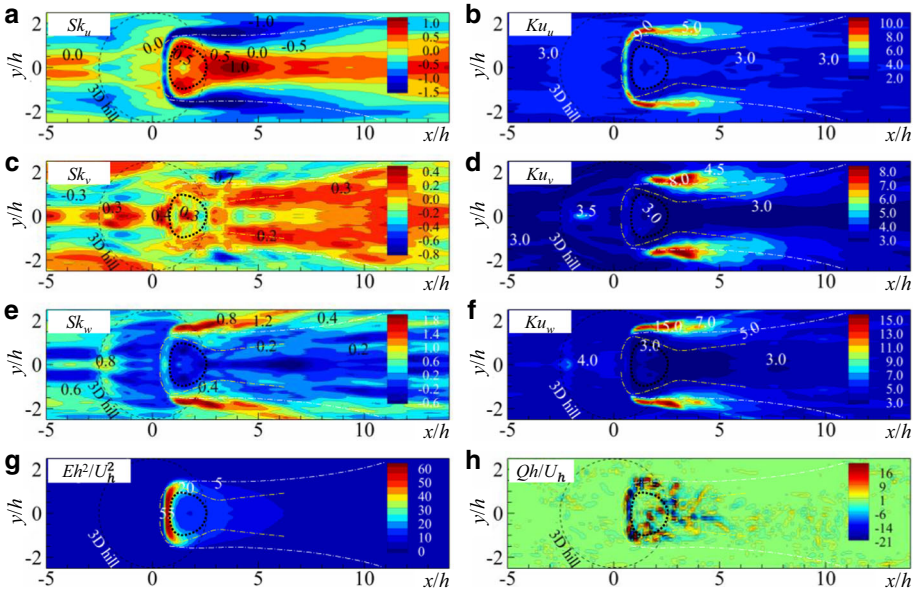

Fig. 11 Contours of skewness of a streamwise Sk_u, **c** spanwise Sk_v, and **e** vertical Sk_w velocity components, and kurtosis of b streamwise Ku_u, **d** spanwise Ku_v, and **f** vertical Ku_w, velocity components, the **g** mean enstrophy, and **h** instantaneous Q-criterion on the plane $z' = 0.25h$. The white and yellow dash–dot lines denote the boundaries of the wake depth and the shear layer, respectively. The thin, black dashed circle indicate the 3D hill. The thick, black dashed lines show the boundary of the separation bubble with zero mean streamwise velocities. The x- and y-axes are normalized by the height h

At the hilltop, the parameters p and u show peak values due to flow separation (Fig. 9b, d), though these peaks are not global maxima, which are instead located at $y = \pm h$, where the normalized p and u values reach 0.12 and 0.35, respectively. Through connecting the crests of the u contours (i.e., the yellow dash–dot line), the region enclosed by the shear layer shrinks after the flow passes the hill, and becomes narrowest at about $x = 3h$, followed by a gentle monotonous expansion. After $x = 7h$, the crests of the u contours gradually disappear. The red dashed circles with a longitudinal width of $1.5h$ and the lateral width of $1.8h$ in Fig. 9 have a zero streamwise velocity component, suggesting recirculation with the remarkably small u_i values as compared with those within the shear layer, and thus a relatively stagnant flow within this recirculation region. The v and w values are large just after the stagnant-flow region, reaching values of $0.28U_h$ and $0.23U_h$ (Fig. 9f, h), respectively.

Within the recirculation circle, the TKE is quite small (Fig. 10a), the values of uw (Fig. 10b) and R_{uw} (Fig. 10f) peak at the centre of the shear layer, uw_{II} values peak almost along the yellow dashed lines (Fig. 10c), while large uw_{IV} values are confined by the shear layer (Fig. 10d), as also identified along the vertical cross-section at $y = 0$ (see Fig. 6c, d). Beyond the neck of the shear-layer region, the ejection area expands, whereas the sweeping area shrinks. The value of Q_{uw} shows that sweeping dominates at the centre of the wake, while ejection dominates within the shear layer.

The skewness Sk_u for the area enclosed by the shear-layer centre is positive, but negative in the shear-layer region (Fig. 11a), with the contour line for $Sk_u = 0$ matching the central line of the shear layer denoted by the yellow dashed lines. The skewness Sk_w has the same pattern as Sk_u (Fig. 11e) and the non-zero value of Sk_v at the wake centre is simply due to our short

sampling time (Fig. 11c). Outside of the wake, however, the value of Sk_v becomes negative, and approaches its maximum at $x = 3h$ and $y = \pm 2h$. The skewness Sk_{u_i} shows a consistent pattern, with peak values found along the wake boundary (Fig. 11a, c and e). Both the peak values for Ku_u and $Ku_v \approx 8$ (Fig. 11b, d), which is approximately half the peak Ku_w value, implying that the shape of the p.d.f. for the vertical velocity component is much steeper than those of the streamwise and spanwise velocity components, or, in another words, the mixing of the vertical velocity component is not as complete as for the horizontal velocity components.

Large enstrophy values mostly concentrate at the separation line, before reducing quickly with downstream distance (Fig. 11g). The contour of Q indicates large eddies wandering laterally and forming a kind of von Kármán vortex street. Together with the enstrophy Q at $y = 0$, the large eddies not only wander up and down but also laterally in a periodic pattern, as confirmed more clearly from the 3D view of Q shown in Sect. 3.4. Note that the points P1–P4 do not appear on $z' = 0.25h$, suggesting that the correlations at the locations h removed from the reference points approach vertically almost a value of zero (Fig. 8).

In general, the data on the plane $z' = 0.25h$ demonstrate highly 3D flow statistics. High values of the parameters u, Sk_{u_i} and Ku_{u_i} concentrate in the shear-layer region consistent with the data on the plane $y = 0$. Interestingly, sweep events dominate at the centre of the wake, while ejection events dominate within the shear layer. In the separation region, due to the existence of the recirculation bubble, the velocity components u and w are largely negatively correlated at the upper bubble boundary, and high values of R_{uw} are concentrated within the shear layer downstream of the hill.

3.4 Flow Characteristics on the Plane $z' = 1.25h$

To understand the extent to which the observed features of the flow on the plane $z' = 0.25h$ reach higher elevations, the flow characteristics on the plane $z' = 1.25h$ are discussed below. On this surface, the magnitudes of speed-up of the values of V and W become almost negligible (Fig. 12e, g), though the speed-up for the value of U remains, indicating an almost constant W profile at the hilltop and a large region with high W values (Fig. 12g). Note that the wake zone is still present, but the separation bubble disappears, and the shear layer becomes weakened on the plane $z' = 1.25h$ (compare Fig. 9 with Fig. 12). Unlike the fluctuations on the plane $z' = 0.25h$, all fluctuation peaks concentrate along the line $y = 0$, showing the maxima at about $x = 4h$, except for the value of p with its maximum at about $x = 2.5h$ (Fig. 12b, d, f, h). The values of these maxima on $z' = 1.25h$ are approximately half of those on $z' = 0.25h$ due to the decreased influence of the hill. The value of uw is confined to the wake region bounded by the white dash–dot lines. Ejections dominate sweeps with the largest ejections at $x = 4h$. Negative values of R_{uw} are present throughout the plane $z' = 1.25h$ even upstream of the hill where the value of R_{uw} is positive on $z' = 0.25h$ (Fig. 13f). The distribution patterns for the skewness Sk_u and Sk_w are almost the same, but with opposing signs (Fig. 14a, e) similar to those on the plane $z' = 0.25h$ (Fig. 11a, e). Positive and negative Sk_v values centred on the plane $z' = 1.25h$ are well organized as compared with those on the plane $z' = 0.25h$. The extension of the peaks for the skewness Sk_u and Sk_w, and the kurtosis Ku_{u_i} along the boundary of the wake region are reduced on the plane $z' = 1.25h$ compared with the plane $z' = 0.25h$ (compare Fig. 11 with Fig. 14). When comparing the values of E and Q on the plane $z' = 1.25h$ with those on the plane $z' = 0.25h$, the three large vortices are still identified, but the Q values are largely reduced, indicating a reduction in the vortex rotation intensity.

The widths of both R_{uu}(P1) and R_{uu}(P2) contours are on approximately the same scale as the height (Fig. 15a, b), indicating an almost circular contour on the y–z cross-section (Fig. 8a,

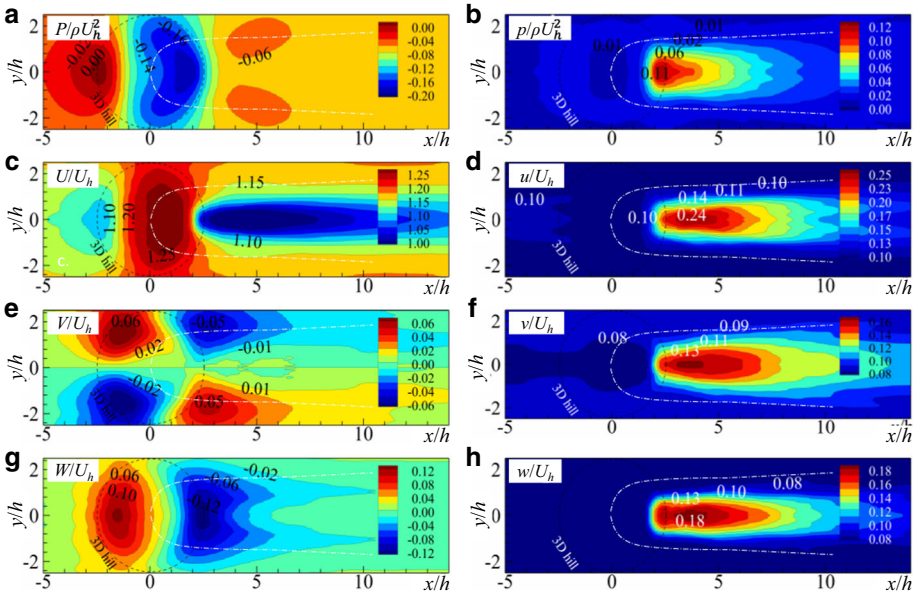

Fig. 12 Contours of mean and fluctuating flow parameters: **a** mean and **b** r.m.s. pressure, the **c** mean and **d** r.m.s. streamwise, **e** mean and **f** r.m.s. spanwise, and **g** mean and **h** r.m.s. vertical velocity components on the plane $z' = 1.25h$. The black dashed circle indicates the 3D hill. The white dash–dot lines denote the boundaries of the wake depth. The x- and y- axes are normalized by the height h

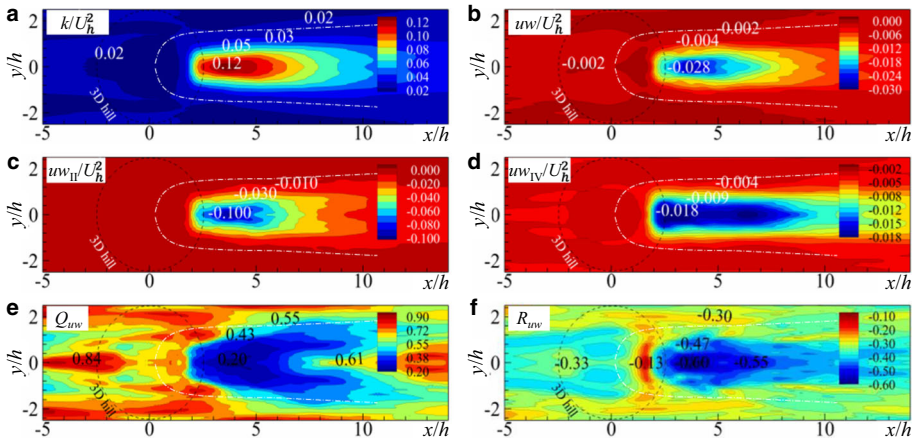

Fig. 13 Contours of the normalized **a** TKE, **b** vertical momentum flux uw, **c** vertical momentum flux in the second quadrant uw_{II}, **d** vertical momentum flux in the fourth quadrant uw_{IV}, **e** the ratio between the vertical momentum flux in the fourth and second quadrants Q_{uw}, and **f** correlation coefficient between streamwise and vertical velocity components R_{uw} on the plane $z' = 1.25h$. The black dashed circle indicates the 3D hill. The white dash–dot lines denote the boundary of the wake depth. The x- and y- axes are normalized by the height h

b). Additionally, the closely-packed contours of R_{uu} values to the right and sparsely-packed contours to the left of the point P2 indicate the presence of high wind speeds and turbulence structures with large coherence. The large decrease in R_{uu}(P3) values with x, but still equal

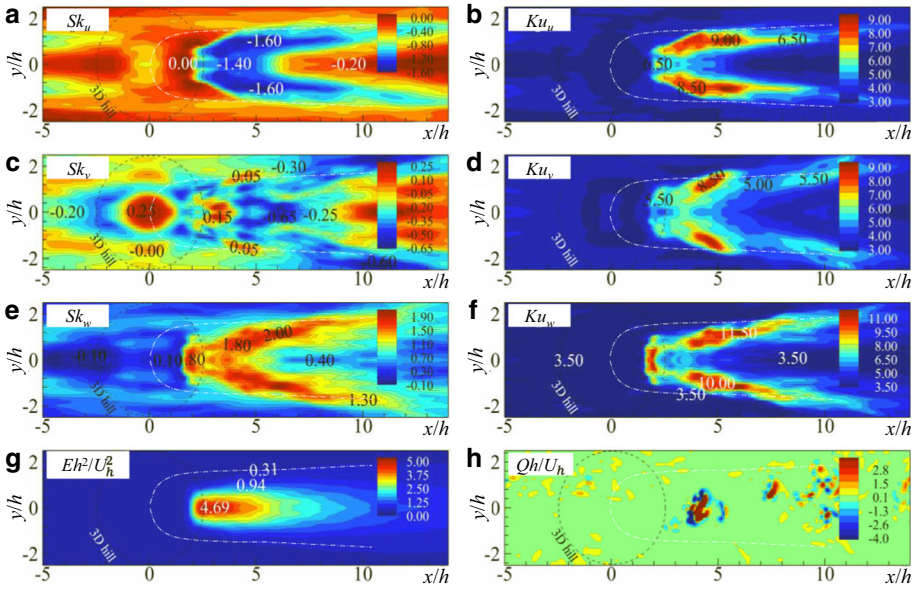

Fig. 14 Contours of skewness of a streamwise Sk_u, **c** spanwise Sk_v, **e** vertical Sk_w velocity components, and kurtosis of b streamwise Ku_u, **d** spanwise Ku_v, and **f** vertical Ku_w velocity components, the **g** mean enstrophy, and **h** instantaneous Q-criterion on the plane $z' = 1.25h$. The black dashed circle indicates the 3D hill. The white dash–dot lines denote the boundary of the wake depth. The x- and y-axes are normalized by the height h

to that on the plane $y = 0$, indicates a large reduction of the wind speed and a strong mixing (Fig. 15g). The magnitude of the correlation then increases with distance x as reflected by the R_{uu}(P4) values (Fig. 15h). When compared with the R_{vv} values on the plane $y = 0$ in Fig. 15c, d, i, j, the contour of R_{vv} values on $z = 1.25h$ shows an elliptical shape, with more correlations in the y-direction than in the z-direction. The value of R_{vv}(P1) increases rapidly when approaching the upstream foothill, before exhibiting a smooth reduction from the foothill to the hilltop (Fig. 15c). However, R_{vv}(P2) values show the reverse pattern (Fig. 15d). After the flow passes the hilltop (Fig. 15i), the values of R_{vv} show roughly a circular pattern, and do not exhibit a recovery as for the R_{uu} values, indicating the different contributions of turbulence between the x-component and the y-component. The values of R_{ww}(P1) and R_{ww}(P2) have similar contours (Fig. 15e, f), while elliptical R_{ww}(P3) contours are presented with an axis oriented in the y-direction as well as the negative correlation zone to the left, and the positive correlation zone to the right (Fig. 15k), which are associated with the flow rotation in the y-direction (Fig. 7g). At the point P4, the positive circular R_{ww}(P4) contour lines in Fig. 15l and the elliptical R_{ww}(P4) contour lines in Fig. 8l suggest 3D spindle iso-surfaces.

In general, the data on the plane $z' = 1.25h$ give clearly different flow statistics compared with those on the plane $z' = 0.25h$. For example, the turbulent fluctuations and the momentum flux concentrate at the centreline, while the skewness and kurtosis peak values are found in the region enclosed by the boundary of the wake depth, since the $z' = 1.25h$ surfaces cross the shear-layer region at the plane $y = 0$. Interestingly, even as the magnitude of the fluctuations decreases with z', the changes in the peak skewness and kurtosis values are not obvious, indicating similar p.d.f. velocities in the shear-layer region regardless of the height.

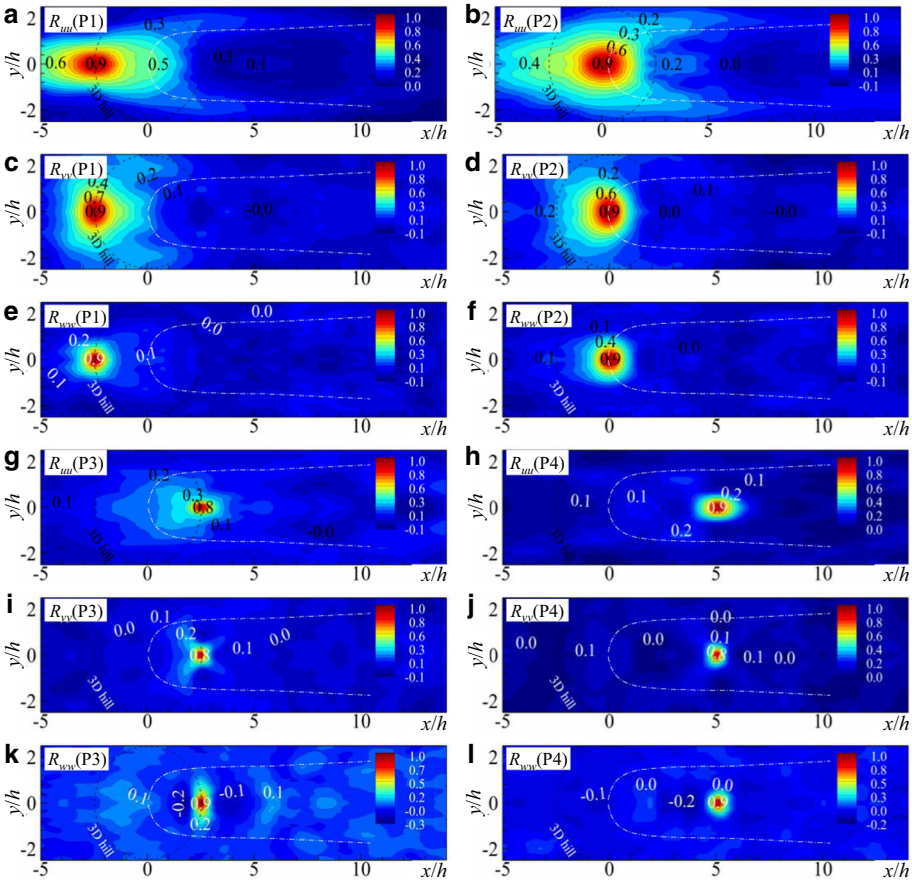

Fig. 15 Contours of the autocorrelation function for the streamwise velocity component R_{uu} computed for the reference points **a** P1, **b** P2, **g** P3, **h** P4, spanwise velocity component R_{vv} computed for the reference points **c** P1, **d** P2, **i** P3, **j** P4, and vertical velocity R_{ww} computed for the reference points **e** P1, **f** P2, **k** P3, **l** P4, on the plane $z' = 1.25h$. The red points show the locations of the reference points. The black dashed circle indicates the 3D hill. The white dash–dot lines denote the boundary of the wake depth. The x- and y-axes are normalized by the height h

3.5 Three-Dimensional View of the Instantaneous Flow Fields

The instantaneous 3D flow fields using Q iso-surfaces enable demonstration of the 3D influence of the hill on the flow as shown in Fig. 16, with an isometric view in Fig. 16a, and a top view in Fig. 16b. The green solid line connects the hilltop with the points $[x, y, z] = [0, 0, h]$ and $[x, y, z] = [10h, 0, h]$, and the white, dashed spiral line, which is determined by the velocity-gradient eigenmode method, illustrates the major core centre of the vortex downstream of the hill. The values of L_1 and L_2 show the spanwise distance from the vortex centre to the green solid line at $x = 3.5h$ and $x = 6.5h$, respectively, and D_1 and D_2 are the vertical distances, respectively. Vertical periodic shedding is expected to provide the negative correlations for the vertical velocity component as discussed in Sect. 3.1. Additionally, there are secondary rotations in the wake flow, as illustrated by the yellow dashed lines with the arrows denoting the rotation direction. These secondary rotations suggest that, when the flow

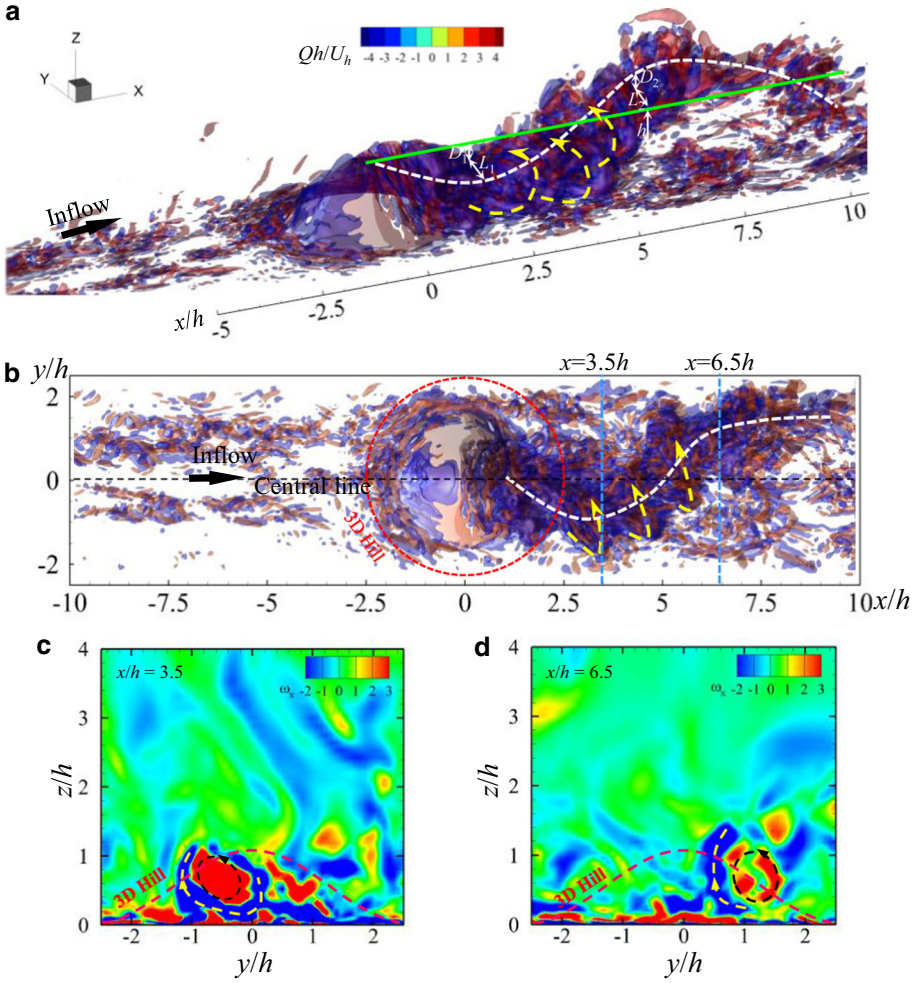

Fig. 16 Instantaneous flow fields visualized by Q-criteria from, **a** isometric, and b the top view. The transparent effects are used for the iso-surfaces of Q values to show the flow structures. The green solid line starts from the hilltop (i.e., $x = [0h, 10h]$, $y = 0$, $z = h$). The white dashed line in Fig. 15a, b locates the major core of the vortex downstream of the hill. The yellow dashed lines indicate the secondary rotation of the wake flow. The red dashed line denotes the boundary of the 3D hill and the thick arrow shows the flow direction. The two blue lines are the locations of the vertical slices of the x component of vorticity, L_1 and L_2 show the spanwise distance from the vortex centre to the green solid line at $x = 3.5h$ and $x = 6.5h$, respectively, and D_1 and D_2 are the vertical distances, respectively. Distributions of the vorticity of the x-component ω_x on the plane of c $x = 3.5h$ and d $x = 6.5h$. The red dashed lines in Fig. 15c, d denote the 3D hill. The x-, y-, and z-axes are normalized by the height h

in the upper part of the wake region moves in a positive y-direction, the flow in the lower part moves in the negative y-direction. As a result, the negative R_{vv}(P3) and R_{vv}(P4) values in the lower part of the wake flow are observed (Fig. 8i, j), which also lead to the two peaks in the vertical profiles of the v velocity component.

Instantaneous flow structures may be examined on the planes $x = 3.5h$ and $x = 6.5h$ using the vorticity of the x-component $\omega_x = \partial\tilde{u}/\partial y - \partial\tilde{v}/\partial x$ (Fig. 16c, d), with red positive and blue negative values. The red dashed lines show the hill shape. The core of the vortex at x

$= 3.5$ is separated into two major regions, including inner rotation with positive ω_x values, and the outer rotation with negative ω_x values. This feature is still clearly visible at $x = 6.5h$, with the lateral location of the core centre moving from $0.5h$ at $x = 3.5h$ to nearly h at $x = 6.5h$, further validating the existence of the lateral periodic wake shedding.

4 Conclusions

The 3D mean and turbulent flows over a hill were simulated and analyzed to yield the following conclusions.

1. The wake depth increases relatively rapidly from $x = 0$ to $x = 5h$, and experiences a gentle increase as x increases. The height of the shear layer decreases slightly from the hilltop to $x = 2.5h$, and then increases at a rate greater than the increased rate for the wake depth. The shear layer on the plane $z = 0.25h$ shrinks after the flow passes the hilltop, becoming narrowest at approximately $x = 3h$, and expanding gradually as x increases.
2. A flow separation with circulation clearly develops downwind of the hill with a negative correlation of u and w values as a result of the convergence of the lateral flows, and the streamwise flow passing over the hilltop.
3. Beyond the neck region of the shear layer, the ejection area expands, whereas the sweeping area shrinks; sweeps dominate in the centre of the wake, and ejections dominate in the shear layer.
4. The major vortex is not just a horizontally-orientated tube structure, but a spirally-shaped structure wandering in both the lateral and vertical directions. In addition, the secondary rotations are identified in the wake flow, leading to the two peaks in the vertical profiles of the v component observed in many studies, and the negative R_{vv}(P3) values near the ground. Another interesting feature is that the core of the vortex is separated into two regions, with the inner rotation having positive ω_x values, and the outer rotation with negative ω_x values.

Acknowledgements Z. Liu acknowledges the support by the National Key Research and Development Plan of China (2016YFE0127900 and 2016YFC0800206), the National Natural Science Foundations of China (51608220), and the Project of Innovation-driven Plan in Huazhong University of Science and Technology (2017KFYXJJ141). S. Cao acknowledges support by the National Natural Science Foundations of China (51720105005). H. Liu acknowledges support by the National Science Foundation (NSF-AGS-1419614).

References

Ansys Inc (2014) Ansys fluent 14.0 user's. Guide, U.S

Baker CJ (2010) The simulation of unsteady aerodynamic cross wind forces on trains. J Wind Eng Ind Aerodyn 98:88–99

Bédard J, Yu W, Gagnon Y, Masson C (2013) Development of a geophysic model output statistics module for improving short-term numerical wind predictions over complex sites. Wind Energy 16:1131–1147

Cao S, Tamura T (2006) Experimental study on roughness effects on turbulent boundary layer flow over a two-dimensional steep hill. J Wind Eng Ind Aerodyn 94:1–19

Carvalho AC, Carvalho A, Gelpi I, Barreiro M, Borrego C, Miranda AI, Pérez-Muñuzuri V (2006) Influence of topography and land use on pollutants dispersion in the atlantic coast of iberian peninsula. Atmos Environ 40:3969–3982

Castro FA, Silva C, Lopes C (2014) One-way mesoscale–microscale coupling for the simulation of atmospheric flows over complex terrain. Wind Energy 18:1251–1272

Courant R, Friedrichs K, Lewy H (1928) Über die partiellen differenzengleichungen der mathematischen physik. Math Annal 100:32–74

Davenport AG, King J (1990) The influence of topography on the dynamic wind loading of long span bridges. J Wind Eng Ind Aerodyn 36:1373–1382

DeLeon R, Sandusky M, Senocak I (2018) Simulations of turbulent flow over complex terrain using an immersed-boundary method. Boundary-Layer Meteorol 167:399–420
Dupont S, Brunet Y (2008) Edge flow and canopy structure: a large-eddy simulation study. Boundary-Layer Meteorol 126:51–71
Ferziger JH, Peric M (2002) Computational method for fluid dynamics. Springer, Berlin
Gong W, Ibbetson A (1989) A wind tunnel study of turbulent flow over model hills. Boundary-Layer Meteorol 49:113–148
Gong W, Taylor PA, Dornbrack A (1996) Turbulent boundary-layer flow over fixed aerodynamically rough two-dimensional sinusoidal waves. J Fluid Mech 312:1–37
Hancock PE, Hayden P (2018) Wind-tunnel simulation of weakly and moderately stable atmospheric boundary layers. Boundary-Layer Meteorol 168:29–57
Hunt J, Carruthers D (1990) Rapid distortion theory and the 'problems' of turbulence. J Fluid Mech 212:497–532
Iizuka S, Kondo H (2004) Performance of various sub-grid scale models in large-eddy simulations of turbulent flow over complex terrain. Atmos Environ 38:7083–7091
Iizuka S, Kondo H (2006) Large-eddy simulations of turbulent flow over complex terrain using modified static eddy viscosity models. Atmos Environ 40:925–935
Ishihara T, Hibi K (1998) An experimental study of turbulent boundary layer over steep hills. In: Proceedings of the 15th national symposium on wind engineering, Japan, pp 61–66
Ishihara T, Oikawa S, Hibi K (1999) Wind tunnel study of turbulent flow over a three-dimensional steep hill. J Wind Eng Ind Aerodyn 83:95–107
Ishihara T, Fujino Y, Hibi K (2001) A wind tunnel study of separated flow over a two-dimensional ridge and a circular hill. J Wind Eng 89:573–576
Kaimal JC, Finnigan JJ (1994) Atmospheric boundary layer flows. Oxford University Press, Oxford
Kutter E, Yi C, Hendrey G, Liu H, Eaton T, Ni-Meister W (2017) Recirculation over complex terrain. J Geophys Res Atmos 122:6637–6651
Liu Z, Ishihara T, Tanaka T, He X (2016) LES study of turbulent flow fields over a smooth 3D hill and a smooth 2-D ridge. J Wind Eng Ind Aerodyn 153:1–12
Lopes AMG, Cruz MG, Viegas DX (2002) Firestation—an integrated software system for the numerical simulation of fire spread on complex topography. Environ Model Softw 17:269–285
Ma Y, Liu H (2017) Large-eddy simulations of atmospheric flows over complex terrain using the immersed-boundary method in the weather research and forecasting model. Boundary-Layer Meteorol 165:421–445
Mason PJ, Thomson DJ (1987) Large-eddy simulations of the neutral-static-stability planetary boundary layer. Q J R Meteorol Soc 113:413–443
Matusick G, Ruthrof KX, Brouwers NC, Hardy GSJ (2014) Topography influences the distribution of autumn frost damage on trees in a mediterranean-type eucalyptus forest. Trees 28:1449–1462
Perdikaris GA (2001) Numerical simulation of the three-dimensional micro-scale dispersion of air-pollutants in regions with complex topography. Heat Mass Transf 37:583–591
Politis ES, Prospathopoulos J, Cabezon D, Hansen KS, Chaviaropoulos PK, Barthelmie RJ (2012) Modeling wake effects in large wind farms in complex terrain: the problem, the methods and the issues. Wind Energy 15:161–182
Raupach MR, Antonia RA, Rajagopalan S (1991) Rough-wall turbulent boundary layers. Appl Mech Rev 44:1–25
Şen Z (2003) A short physical note on a new wind power formulation. Renew Energy 28:2379–2382
Shaw RH, Brunet Y, Finnigan JJ, Raupach MR (1995) A wind tunnel study of air flow in waving wheat: two-point velocity statistics. Boundary-Layer Meteorol 76:349–376
Shekar A, Graham M (2018) Exact coherent states with hairpin-like vortex structure in channel flow. J Fluid Mech 849:76–89
Su HB, Shaw RH, Paw UKT (2000) Two-point correlation analysis of neutrally stratified flow within and above a forest from large-eddy simulation. Boundary-Layer Meteorol 94:423–460
Tamura T, Cao S, Okuno A (2007a) LES study of turbulent boundary layer over a smooth and a rough 2D hill model. Flow Turbul Combust 79:405–432
Tamura T, Okuno A, Sugio Y (2007b) LES analysis of turbulent boundary layer over 3D steep hill covered with vegetation. J Wind Eng Ind Aerodyn 95:1463–1475
Tian S, Gao Y, Dong X, Liu C (2018) Definitions of vortex vector and vortex. J Fluid Mech 849:312–339
Zilker D, Cook G, Hanratty T (1977) Influence of the amplitude of a solid wavy wall on a turbulent flow. Part 1. Non-separated flows. J Fluid Mech 82:29–51